Geophysical Prospecting

EAGE EUROPEAN ASSOCIATION OF GEOSCIENTISTS & ENGINEERS

Geophysical Prospecting, 2018, **66**, 1384–1401 doi: 10.1111/1365-2478.12643

Laboratory measurements of seismic attenuation and Young's modulus dispersion in a partially and fully water-saturated porous sample made of sintered borosilicate glass

Samuel Chapman[1]*, Beatriz Quintal[1], Klaus Holliger[1], Lukas Baumgartner[1] and Nicola Tisato[2,3]

[1]*Institute of Earth Sciences, University of Lausanne, Lausanne, Switzerland,* [2]*Department of Geological Sciences, Jackson School of Geosciences, the University of Texas at Austin, Austin, USA, and* [3]*Department of Civil Engineering, University of Toronto, Toronto, Canada*

Received July 2017, revision accepted April 2018

ABSTRACT

We measured the extensional-mode attenuation and Young's modulus in a porous sample made of sintered borosilicate glass at microseismic to seismic frequencies (0.05–50 Hz) using the forced oscillation method. Partial saturation was achieved by water imbibition, varying the water saturation from an initial dry state up to ~99%, and by gas exsolution from an initially fully water-saturated state down to ~99%. During forced oscillations of the sample effective stresses up to 10 MPa were applied. We observe frequency-dependent attenuation, with a peak at 1–5 Hz, for ~99% water saturation achieved both by imbibition and by gas exsolution. The magnitude of this attenuation peak is consistently reduced with increasing fluid pressure and is largely insensitive to changes in effective stress. Similar observations have recently been attributed to wave-induced gas exsolution–dissolution. At full water saturation, the left-hand side of an attenuation curve, with a peak beyond the highest measured frequency, is observed at 3 MPa effective stress, while at 10 MPa effective stress the measured attenuation is negligible. This observation is consistent with wave-induced fluid flow associated with mesoscopic compressibility contrasts in the sample's frame. These variations in compressibility could be due to fractures and/or compaction bands that formed between separate sets of forced-oscillation experiments in response to the applied stresses. The agreement of the measured frequency-dependent attenuation and Young's modulus with the Kramers–Kronig relations and additional data analyses indicate the good quality of the measurements. Our observations point to the complex interplay between structural and fluid heterogeneities on the measured seismic attenuation and they illustrate how these heterogeneities can facilitate the dominance of one attenuation mechanism over another.

Key words: Attenuation, Rock physics.

1. INTRODUCTION

In the seismic frequency range, frequency-dependent wave attenuation and Young's modulus dispersion in fluid-saturated rocks are generally attributed to wave-induced fluid flow (WIFF) arising from compressibility contrasts in the rock (e.g. Müller, Gurevich and Lebedev 2010). The forced oscillation method (e.g. McKavanagh and Stacey 1974) is suitable to experimentally study seismic attenuation in fully and partially saturated rocks. Particular emphasis has recently been given to fully saturated sandstones where the shift of the attenuation peak to lower frequencies with increasing fluid viscosity

*Email: samuel.chapman@unil.ch

and the sensitivity of the attenuation behaviour to structural properties have been observed (Pimenta, Fortin and Gueguen 2015; Subramaniyan *et al.* 2015; Mikhaltsevitch, Lebedev and Gurevich 2016a; Spencer and Shine 2016; Borgomano *et al.* 2017). These observations have largely been attributed to squirt flow, which is a form of microscopic WIFF that occurs between compliant cracks or grain contacts and stiff pores (e.g. Mavko and Jizba 1991; Chapman, Zatspin and Crampin 2002; Gurevich *et al.* 2010). Partial saturation effects in the seismic range were also experimentally studied by a number of authors (e.g. Gautam 2003; Batzle, Han and Hofmann 2006; Adam *et al.* 2009; Mikhaltsevitch, Lebedev and Gurevich 2016b), showing generally an increase in attenuation with saturation. A theoretical model associated with partial saturation is patchy saturation, which is a form of mesoscopic WIFF (White 1975). However at seismic frequencies little focus has been given to the influence of the pore fluid distribution.

At sonic frequencies, Cadoret Marion and Zinszner (1995) and Cadoret, Mavko and Zinszner (1998) linked the fluid distribution observed in X-ray scans, having modified the size of heterogeneities by changing the saturation method, to the measured extensional-mode attenuation. Chapman *et al.* (2017) studied how the fluid distribution affects the scaling of the high-frequency asymptote of bell-shaped attenuation curves measured in a partially saturated Berea sandstone sample at seismic frequencies. For partial water saturation (~99%) achieved by gas exsolution from an initially fully water saturated state, the high-frequency asymptote consistently scaled as $Q^{-1} \propto f^{-1}$. Given the frequency scaling and the expected length scale of the fluid heterogeneities, the frequency-dependent attenuation could not be reconciled with mesoscopic WIFF. Measurements on the same sample for similar levels of water saturation achieved by imbibition were however consistent with mesoscopic WIFF (Chapman *et al.* 2016). Tisato *et al.* (2015) proposed wave-induced gas exsolution–dissolution (WIGED) of pore-scale bubbles in the liquid phase as another mechanism to explain the frequency-dependent attenuation measured at seismic frequencies in partially saturated Berea sandstone with air, nitrogen and carbon dioxide as the gas phase. WIGED may explain the frequency-dependent behaviour observed by Chapman *et al.* (2017) for the saturation procedure based on gas exsolution. However, WIGED has not been widely studied and so far the experimental observations and interpretations of Tisato *et al.* (2015) and Chapman *et al.* (2017) have not been corroborated.

The aim of this study is to complement the work of Tisato *et al.* (2015) and Chapman *et al.* (2017) by providing further laboratory measurements of the anomalous frequency-dependent attenuation using a different type of porous material. A set of forced oscillation experiments were performed in the microseismic to seismic frequency range on a sample made of sintered borosilicate glass, which has a higher porosity but smaller pore size than the sandstone samples used in the previous studies. The sample was chosen because we believed its mono-mineralic composition and homogenous structure would reduce the complexity of the problem. However, due to its mechanical weakness, the sample underwent unintended permanent deformation in the form of compaction bands and fractures. In the following sections we will describe the sample and the permanent deformation that took place between the sets of forced oscillation experiments when the stress imposed on the sample was changed. The results will be presented with respect to the experimental conditions and procedures used. We will show that frequency-dependent attenuation and Young's modulus dispersion are causally linked and therefore cannot be a consequence of the permanent deformation. Then, we will discuss possible interpretations for the resulting frequency-dependent attenuation with respect to known attenuation mechanisms and compare our results with previous experimental observations.

2. EXPERIMENTAL METHODOLOGY

2.1 Attenuation and Young's modulus

The laboratory experiments were carried out in the Broad Band Attenuation Vessel (BBAV) (Tisato and Madonna 2012). The BBAV (Fig. 1) is a triaxial cell that employs the forced oscillation method (e.g. McKavanagh and Stacey 1974) to measure the extensional-mode attenuation Q^{-1} and the real-valued Young's modulus E in the seismic frequency range. A multi-layer piezoelectric stack applies a sinusoidal stress to the sample that is measured by a calibrated load cell. A strain-gauge cantilever sensor measures the resulting bulk axial strain of the sample. The phase shift between stress and strain signals allows for determining the attenuation, while the Young's modulus is obtained from the ratio of the peak-to-peak stress and strain. The dynamic stress produces a strain amplitude of $\sim 10^{-6}$. The measurements are performed at frequencies ranging from 0.05 to 50 Hz. For each pair of attenuation and Young's modulus curves, five measurements are performed at each frequency from which the median and range are determined. Tisato and Madonna (2012) provide further details on the BBAV, including its calibration and the testing of standard samples.

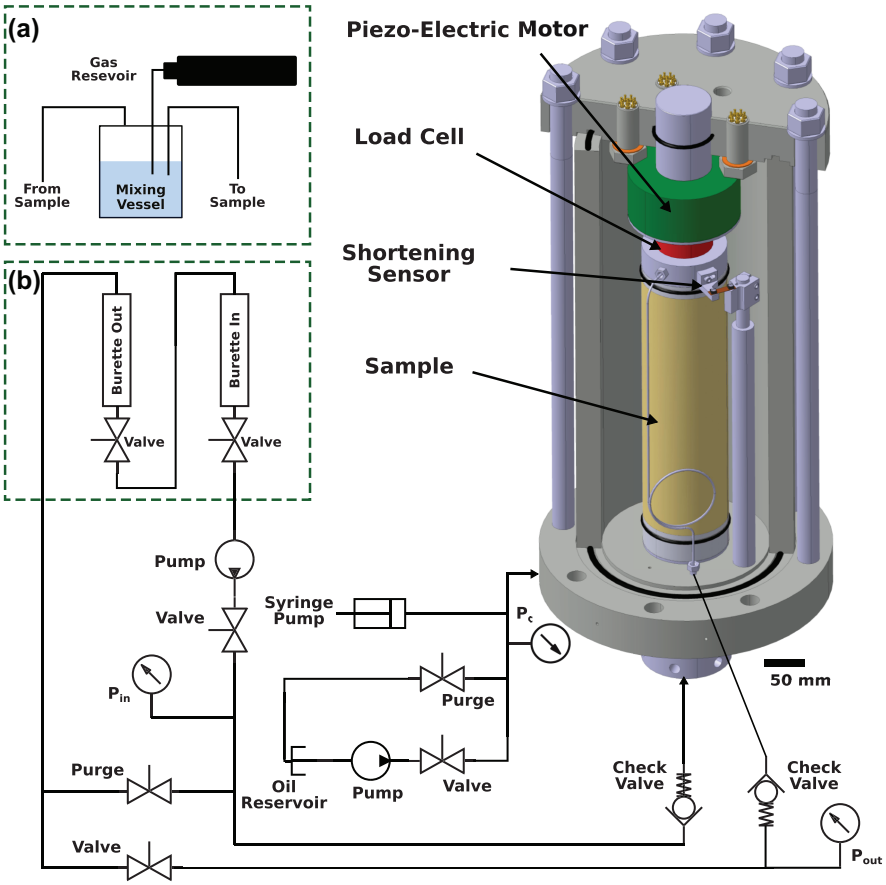

Figure 1 Schematic illustration of the BBAV (Tisato and Madonna 2012) together with a diagram of the pore fluid and confining pressure circuits. The interchangeable insets (a) and (b) describe the setups used for partial water saturation by gas exsolution and by imbibition, respectively. Adapted from Tisato and Madonna (2012).

A pore fluid circuit (Fig. 1) connected to the BBAV allows for controlling the fluid saturation and the fluid pressure in the sample. Graduated burettes are used to measure the volume of fluid injected and expelled during saturation. The difference between these quantities gives the volume of fluid inside the sample. Knowing the sample's pore volume and the volume of injected fluid allows for inferring the degree of saturation. The saturating fluid is introduced into the pore space via the bottom of the sample. Fluid flow out of the sample, induced by the axial compression of the sample during the experiment, can bias the measured attenuation (Gardner 1962; Dunn 1987; Mörig and Burkhard 1989; Pimienta *et al.* 2016). To prevent fluid flow across the sample's boundaries from influencing the measurements, spring loaded check valves in the sample holders prevent the flow into the fluid lines and a layer of glue and aluminium foil cover the curved surface of the cylindrical sample. In addition, a fluorinated ethylene propylene shrink tube isolates the sample from the confining oil.

2.2 Sample description

Two initially identical samples, GL1 and GL2, made of sintered borosilicate glass, were subjected to forced oscillations in the BBAV. The cylindrical samples had a diameter of 76 mm and a length of 250 mm. According to the samples' manufacturer (The Goodfellow Group), the pores had a diameter of $\sim 5\ \mu$m. The first experiments with GL1, involving a maximum effective stress of ~20 MPa and a static axial stress of ~22.2 MPa, deformed and fractured the sample. We define the effective stress σ_{eff} as the difference between the confining pressure P_c and fluid pressure P_f (i.e. $\sigma_{\text{eff}} = P_c - P_f$). Smaller cores were subsequently drilled parallel to the sample's vertical axis to visualize the internal structure with X-ray micro-tomography (micro-CT) (Fig. 2). Thin bands of denser composition, characterized by lighter colour in the micro-CT images, run sub-perpendicular to the vertical axis of the cores (Fig. 2b,c). Mesoscopic fractures radiating out from the

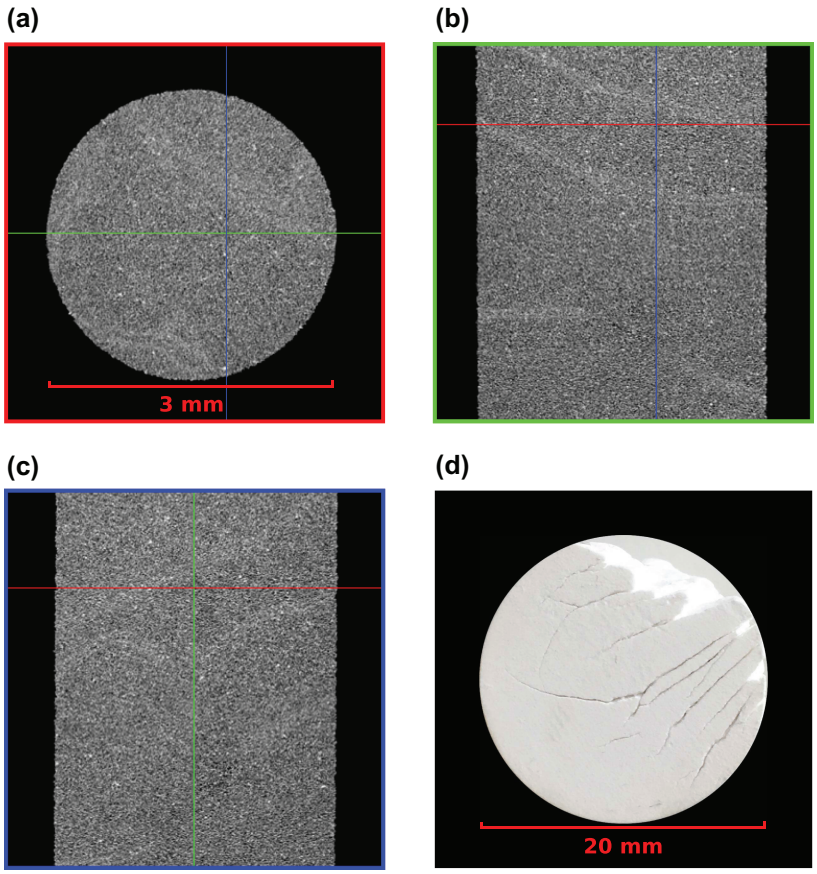

Figure 2 (a), (b) and (c) Micro-CT cross sections of a core with a diameter of 3 mm drilled parallel to the vertical axis of sample GL1. (d) Photograph of the top surface of a core with a diameter of 20 mm drilled parallel to the vertical axis showing fractures radiating from the centre of sample GL1.

sample's centre are also visible (Fig. 2d). The strong deformation forced us to discontinue the experiments with sample GL1 and to start over with sample GL2 and perform the experiments at lower effective and static vertical stresses.

We performed all forced oscillation measurements on sample GL2 at a static axial stress of 1.1 MPa, in addition to the confining pressure, and we did not subject the sample to effective stresses in excess of 10 MPa. A static axial stress was applied on the sample during measurements to ensure the proper coupling between the sample and the piezoelectric motor. Before the measurements, we did, however, impose a static axial stress of ~4 MPa on the sample to compensate for any roughness that may remain after grinding the sample ends and to minimize misalignments in the experimental stack. Visual inspection of the sample between the sets of experiments did, however, reveal again the formation of fractures.

After performing all forced oscillation measurements, the sample was cut perpendicular to its vertical axis into three pieces of roughly equal length that were suitable for micro-CT imaging (Fig. 3). On the bottom of the uppermost piece, two connected fractures are visible (Fig. 3a), which are also visible on the top of the middle piece. The discolouring of the surface is rust from the saw blade (Fig. 3a). The fractures appear to extend almost halfway into the uppermost piece (Fig. 3b) and only a few millimetres into the middle piece. In the micro-CT images, these fractures appear denser than the surrounding pore space, as indicated by their lighter colour, which could be due to rust from the saw blade or debris having been flushed into the fractures. Other, smaller fractures can also be seen in the micro-CT images and are marked by small black arrows in Fig. 3b,c. In Fig. 3b, a vertical section of a cone-shaped region of lower density can be seen, beginning close to the termination point of the connected fractures. In both the upper and middle pieces of the sample, densifications similar to those seen in GL1 are visible sub-perpendicular to the vertical axis of the sample (Fig. 3b,c). The micro-CT images confirm that the internal structure of GL2 was far more heterogeneous than expected and that the sample was permanently deformed over the course of the experiments, however, to a lesser extent than in GL1.

Before performing the attenuation measurements, the water permeability of sample GL1 was determined with a

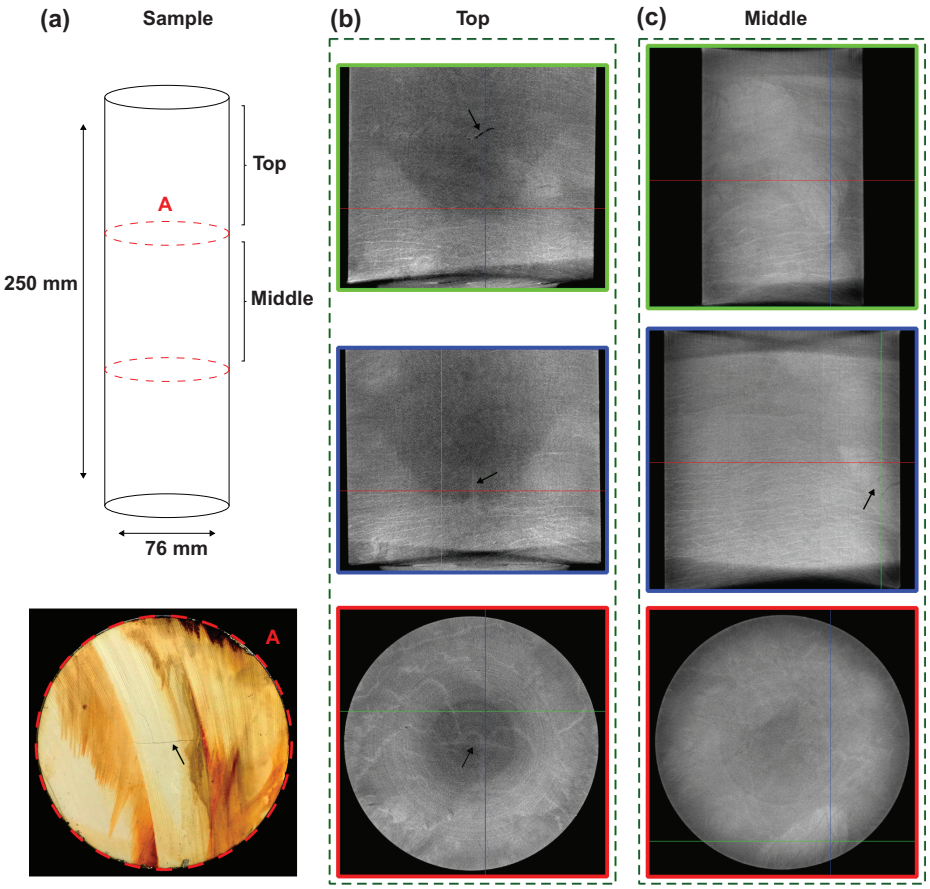

Figure 3 (a) Illustration of the imaged sections of sample GL2 and a photograph of the cut surface of the top piece. X-ray micro-CT cross sections of the (b) upper and (c) middle pieces. The arrows point out some of the fractures in the sample.

Table 1 Permeability and porosity of samples GL1 and GL2 before permanent deformation determined at ambient pressure conditions

Sample	GL1	GL2
Permeability (mD)	152	152 (assumed)
Porosity (%)	47	45

Table 2 Permeability and porosity of sample GL2 after permanent deformation

Sample	GL2			
	Effective stress (MPa)			
	0.15	3	6.5	10
Permeability (mD)	11.6 – 21	2 – 15.9	0.7 – 1.1	0.3
Porosity (%)	44*			

*Measured at ambient pressure conditions

falling head permeability test and the porosity of both samples was determined from the grain density as well as from the samples dimensions and weight (Table 1). Following the attenuation experiments, we measured the permeability and porosity of the three sample pieces of GL2. The porosity was determined at ambient conditions using the dry and saturated sample masses (Table 2). The upper and middle sample pieces were cored to a diameter of ~60 mm parallel to the vertical axis and stacked, one above the other, to increase the length-to-diameter ratio. The pieces were allowed to soak in water for about a week before the permeability was measured in a pressure cell at the four effective stresses that were sustained during the attenuation measurements. By applying a constant fluid pressure gradient across the sample length and measuring the fluid flow we calculated the hydraulic conductivity from which we inferred the sample's permeability. Assuming that the original permeability of sample GL2 was comparable to that of GL1, the permeability was reduced over the course of the experiments by 1 to 2 orders-of-magnitude. The

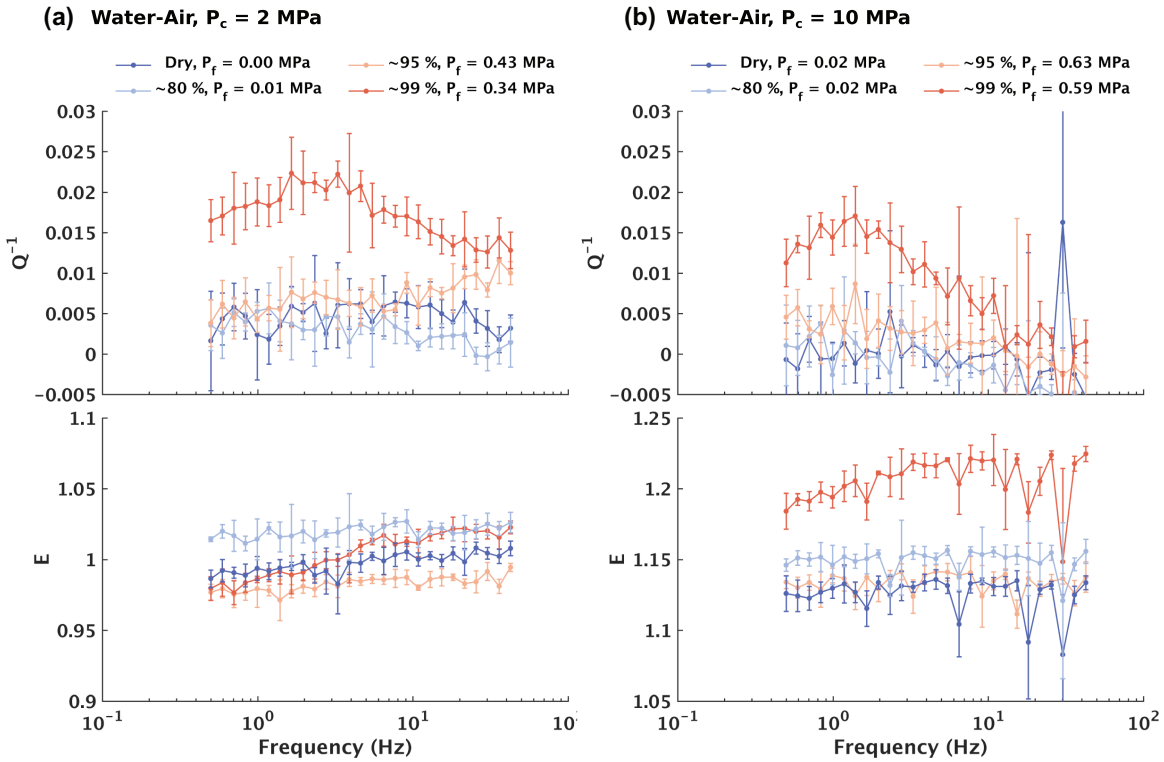

Figure 4 Attenuation Q^{-1} and normalized Young's modulus E at (a) 2 MPa and (b) 10 MPa confining pressure P_c. The Young's moduli are normalized against the mean Young's modulus measured at dry conditions and 2 MPa confining pressure. The legend provides the water saturation and fluid pressure P_f. The gas phase is air.

permeability was also observed to be highly dependent on the effective stress (Table 2). For effective stresses of 0.15, 3 and 6.5 MPa, the permeability was measured again after unloading the sample. The second measured permeability was always lower, which is why we provide the results as a range. The sample proved quite friable when touched. At the contact between the sample and the sample holders we noticed the formation of gouge, which perhaps contributed to the reduction in permeability.

3. RESULTS

In the following subsections, we present the measured attenuation and Young's modulus according to the saturation method instead of the experimental sequence. Each set of experiments is identified by a different saturating gas phase. Between the three sets of experiments, the sample was removed from the BBAV and dried. After drying, the sample was allowed to equilibrate with respect to the laboratory humidity before conducting the next experiments. The experimental sequence started with water–nitrogen, continued with water–air and finished with water–carbon dioxide as the pore fluids.

3.1 Partial water saturation by imbibition

To study the influence of partial saturation on frequency-dependent attenuation and Young's modulus dispersion, we introduced deionized water by imbibition into the base of the air-saturated sample while maintaining a 10 MPa confining pressure. Once the desired saturation of water was reached, the valves of the pore fluid lines were closed. To achieve ~99% water saturation, the fluid pressure in the sample was increased to force the water into the remaining unsaturated pore space. Thus, it is possible that the remaining gas in the pore space partially dissolved into the water and came out of solution again when the pore pressure was reduced before performing the measurements. We measured the attenuation and Young's modulus first at 10 MPa and then at 2 MPa confining pressure. The fluid pressure was not controlled because the pore fluid lines remained closed while we adjusted the confining pressure.

For dry conditions and ~80% water saturation, the attenuation is negligible (Fig. 4a,b). At ~95% water saturation and 2 MPa confining pressure (Fig. 4a), we observe the possible left flank of a bell-shaped attenuation curve. However, at 10 MPa confining pressure (Fig. 4b) the attenuation

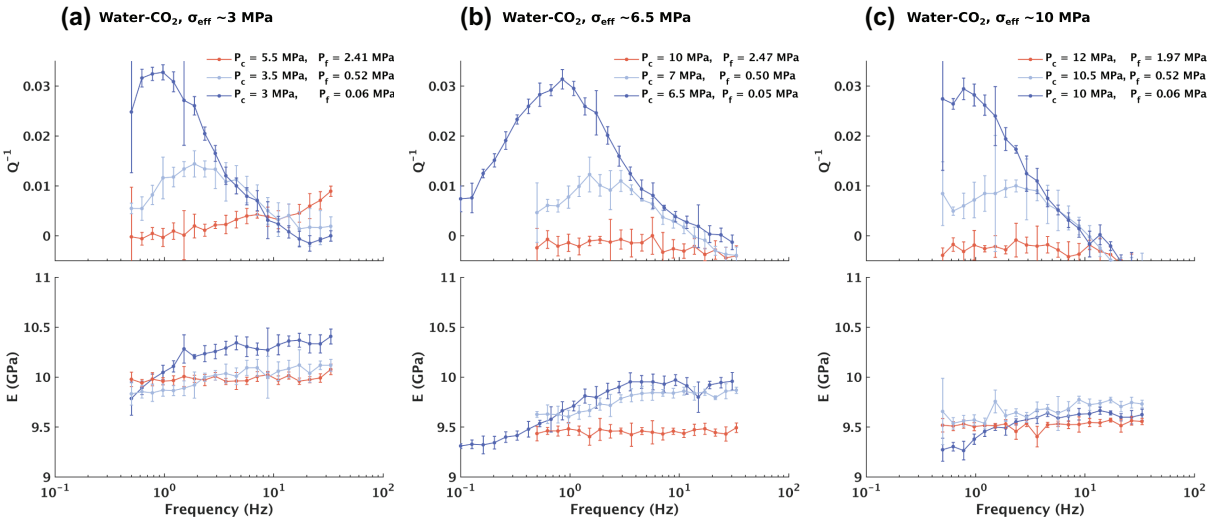

Figure 5 Attenuation Q^{-1} and Young's modulus E near full water saturation at (a) ~3 MPa, (b) ~6.5 MPa and (c) ~10 MPa effective stress σ_{eff}. The legend provides the confining P_c and fluid P_f pressures. The gas phase is carbon dioxide.

is again negligible. Only at ~99% water saturation do we observe significant and frequency-dependent attenuation with a transition frequency at 1–3 Hz. Furthermore, by decreasing the confining pressure from 10 to 2 MPa the attenuation peak increases and the transition frequency shifts to slightly higher frequencies (Fig. 4a,b).

The Young's moduli measured at different saturation and stress levels are normalized against the mean Young's modulus at dry conditions and 2 MPa confining pressure. We were, however, not confident in the calibration of the strain gauge cantilever, that is why we choose to show the normalized value. We observe at 2 MPa confining pressure that the Young's modulus first increases with the introduction of water (Fig. 4a). At ~95% water saturation, the Young's modulus drops again below the value for the dry measurement. Accompanying the attenuation curve there is significant dispersion in the Young's modulus at ~99% water saturation. The Young's modulus at 10 MPa confining pressure (Fig. 4b) first increases with the introduction of water and then decreases again at ~95% water saturation, as was the case at 2 MPa confining pressure. At ~99% water saturation, the Young's modulus is strongly dispersive and significantly larger than at dry conditions. Overall the sample is stiffer at a confining pressure of 10 MPa than at 2 MPa, as expected.

3.2 Partial water saturation by gas exsolution: fluid pressure and effective stress

As opposed to achieving partial water saturation by imbibition (Fig. 4), for the measurements presented in this subsection we allowed the gas dissolved in the water to come out of solution to form homogenously distributed pore-scale gas bubbles (Zuo *et al.* 2017). First, however, we flushed the sample with carbon dioxide. Deionized water, in equilibrium with carbon dioxide at a pressure slightly above atmospheric pressure, was then pumped into the sample. The sample was flushed with multiple pore volumes of water. To fully saturate the sample and to dissolve any remaining gas into the water, the fluid pressure in the sample was raised above 2 MPa. Subsequently, we first lowered the confining pressure on the sample and then opened the outlet valve of the pore fluid line, allowing the gas to exsolve. When opening the pore fluid line, only a few drops of water were expelled. Given the large pore volume of the sample (>500 ml), this indicates a subsequent gas saturation of less than 1%. The attenuation and Young's modulus were measured at various effective stresses and fluid pressures. Before these measurements were conducted the strain-gauge cantilever was recalibrated, that is why the Young's moduli are presented as absolute values.

Generally, the measured frequency-dependent attenuation with a transition frequency between 1 and 5 Hz is independent of the effective stress, but sensitive to the fluid pressure (Fig. 5). For fluid pressures >2 MPa, the attenuation is negligible at effective stresses of ~6.5 MPa (Fig. 5b) and ~10 MPa (Fig. 5c). However, at ~3 MPa effective stress and 2.41 MPa fluid pressure the attenuation is slightly frequency dependent and we observe the possible left-hand side of a bell-shaped attenuation curve (Fig. 5a). The attenuation is

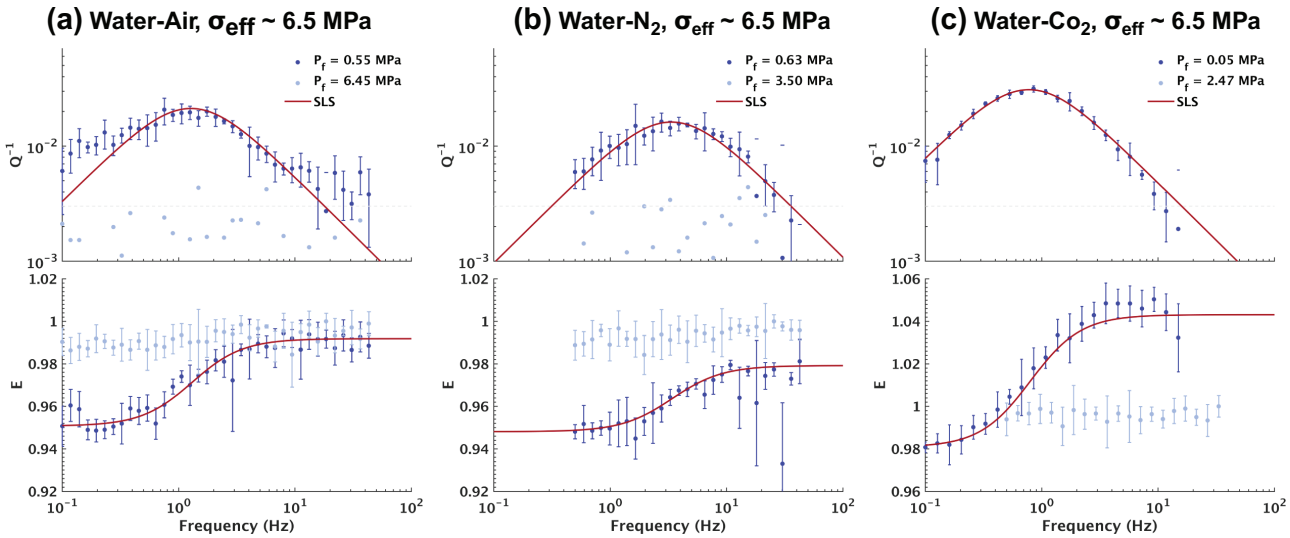

Figure 6 Attenuation Q^{-1} and normalized Young's modulus E near full water saturation and a constant effective stress σ_{eff} of ~6.5 MPa. Three different gas phases are considered: (a) air, (b) nitrogen and (c) carbon dioxide. The legend provides the fluid pressures P_{f}. The red line denotes the fit of the SLS model. The grey shaded area marks the limit of the measurement sensitivity.

increasingly frequency dependent as we lower the fluid pressure, with transition frequencies at 2–3 Hz and 0.5 MPa fluid pressure. The attenuation is maximal at the lowest fluid pressure, which is close to ambient pressure, with a transition frequency at 0.7–1 Hz.

Overall, the Young's modulus decreases with increasing effective stress, though the variation is minimal at ~1.5 GPa (Fig. 5). For all effective stresses, the Young's modulus measured at the lowest fluid pressures is greater than the Young's modulus measured at the highest fluid pressures, at least at frequencies that are higher than the transition frequency.

3.3 Partial water saturation by gas exsolution: different gases

We employed the same experimental procedure as in the previous subsection for carbon dioxide (Fig. 5) to study the influence of the gas type on attenuation. We considered air and nitrogen as the gas phases and performed the measurements at an effective stress of ~6.5 MPa. We measured the attenuation first at the highest fluid pressure.

The attenuation for water–air (Fig. 6a) and water–carbon dioxide (Fig. 6c) both have a transition frequency at ~1 Hz, while the attenuation for water–nitrogen (Fig. 6b) has a transition frequency at ~4 Hz. We fit the results with a standard linear solid (SLS) model for a single relaxation time (Zener 1948; Liu, Anderson and Kanamori 1976), by performing a non-linear least-squares regression to the attenuation data. In the three cases, the SLS fits well the high-frequency asymptote of the measured attenuation. For the water–air case, the SLS deviates from the measured attenuation at low frequencies (Fig. 6a). For fluid pressures >2.5 MPa the attenuation is negligible, including for the case of water–carbon dioxide (Fig. 6c), which can be observed in Fig. 5b with a linear scale for the y-axis.

The Young's moduli measured are normalized to allow for directly comparing the results of the three sets of experiments. At fluid pressures >2.5 MPa, there is negligible dispersion of the Young's modulus. For water–air (Fig. 6a) and water–nitrogen (Fig. 6b) the Young's modulus shows significant dispersion at low fluid pressures and is overall lower than when measured at higher fluid pressures. However, for water–carbon dioxide (Fig. 6c), the dispersive Young's modulus at low fluid pressure is greater than when it is measured at high fluid pressure, as observed already in Fig. 5.

4. DISCUSSION

4.1 Sample deformation

Based on the visual inspection of the sample between sets of experiments, it was evident that the sample had yielded under the applied stresses. The densifications sub-perpendicular to the sample's vertical axis (Fig. 3) resemble compaction bands

formed by pore space collapse (Wong, Baud and Klein 2001). This interpretation is supported by the fact that the bulk permeability of sample GL2 was an order-of-magnitude lower than that of the original intact sample and was sensitive to the effective stress (Table 1) (Holcomb and Olsson 2003; Vajdova, Baud and Wong 2004). However, neither the visual inspection of the sample between the sets of experiments nor the micro-CT images indicates how the deformation progressed. The reduction in Young's modulus with increasing effective stress (Fig. 5) suggests that the sample deformed as the confining and fluid pressures were adjusted. This raises the question of whether the sample also deformed in response to the forced oscillation.

The frequency-dependent attenuation and Young's modulus are determined independently from each other. It is therefore common to use the causality principle to verify the consistency of the data (e.g. Mikhaltsevitch *et al.* 2016a) by using either the Kramers–Kronig relations or a rheological model that satisfies this principle, such as the SLS model. The good fit of the SLS model to the attenuation and Young's modulus from the three sets of experiments (Fig. 6), between which the sample was dismounted from the vessel, indicates that the data are generally consistent with the causality principle. A simplified formulation of the Kramers–Kronig relations (Mikhaltsevitch *et al.* 2016a) is applied to the data at ~99% water saturation and 2 MPa confining pressure (Fig. 8a). However, as can be seen in the data set presented in Fig. 6b, between 10 and 30 Hz, there are instances where the measured Young's modulus has a broad range of values and departs significantly from the general trend. Only in these instances, it is likely that the forced oscillation is inducing some failure in the sample, and we correspondingly observe in the stress–strain signal that, at these frequencies, the strain does not recover from the applied stress. Appendix A provides details on the stress–strain response of the sample and the observed variations of the attenuation and the Young's modulus over the five measurements cycles performed for each experiment. Overall, the measurements at the given experimental conditions are reliable and in agreement with the causality principle. However, as the experimental conditions are adjusted (e.g. Fig. 5) the solid frame of the sample is permanently deformed. Interpreting how changes in the experimental conditions influence the observed attenuation and Young's modulus becomes difficult. Thus, the following analysis, when it is strongly concerned with the solid frame of the sample, only lays out some possible explanations for the observations and should not be taken as a definite interpretation.

4.2 WIFF: fluid heterogeneities

Attenuation induced by WIFF in response to a patchy fluid distribution (White 1975) is dependent on a number of properties. Of particular importance to the experiments presented here are the distribution and size of fluid heterogeneities, sample permeability and the applied effective stress (Dutta and Seriff 1979). For example, by increasing the size of the water heterogeneities the attenuation peak will shift towards lower frequencies, as has been observed by Chapman *et al.* (2016) when increasing the size of the water patches by imbibition in an otherwise air-saturated sample. Similar observations have been reported by Spencer and Shine (2016) who conducted experiments with brine-saturated samples into which they injected supercritical carbon dioxide. Similarly, a reduction of a sample's permeability would shift the attenuation peak to lower frequencies, while an increase in effective stress should increase a sample's stiffness, which, in turn, would reduce the magnitude of the attenuation peak.

Tisato and Quintal (2013) and Chapman *et al.* (2016) attributed the frequency-dependent attenuation in Berea sandstone samples of similar dimensions and permeability to GL2, for water saturation levels larger than 60% achieved by imbibition, to WIFF in response to a patchy fluid distribution. However, the frequency-dependent attenuation of sample GL2, measured at low fluid pressures and characterized by transition frequencies between 1 and 5 Hz, is only observed for water saturation levels of ~99% (Figs. 4 and 6), regardless of the saturation method used. Partial saturation achieved by imbibition is expected to produce larger fluid heterogeneities compared with a homogeneous exsolution of gas bubbles and therefore produce a shift in the attenuation peaks with respect to frequency. However this is not observed and as a consequence, mesoscopic WIFF in response to a patchy fluid distribution cannot readily explain the bell-shaped attenuation curves presented in Figs. 4, 5 and 6.

Considering that the formation of compaction bands likely progressively reduced the bulk permeability of sample GL2, attenuation in response to WIFF related to patchy saturation could be significant at frequencies below 0.5 Hz. In Fig. 7a, we show the attenuation measured from 0.05 to 50 Hz, at ~90% water saturation and 2 MPa confining pressure, together with the results for White's 1D analytical solution for a rock with a periodic pore fluid distribution (White, Mikhaylova and Lyakhovitskiy 1975). The analytical solution is only used to provide a rough idea of the frequency range in which one might expect to observe frequency-dependent attenuation caused by WIFF due to patchy saturation. Note

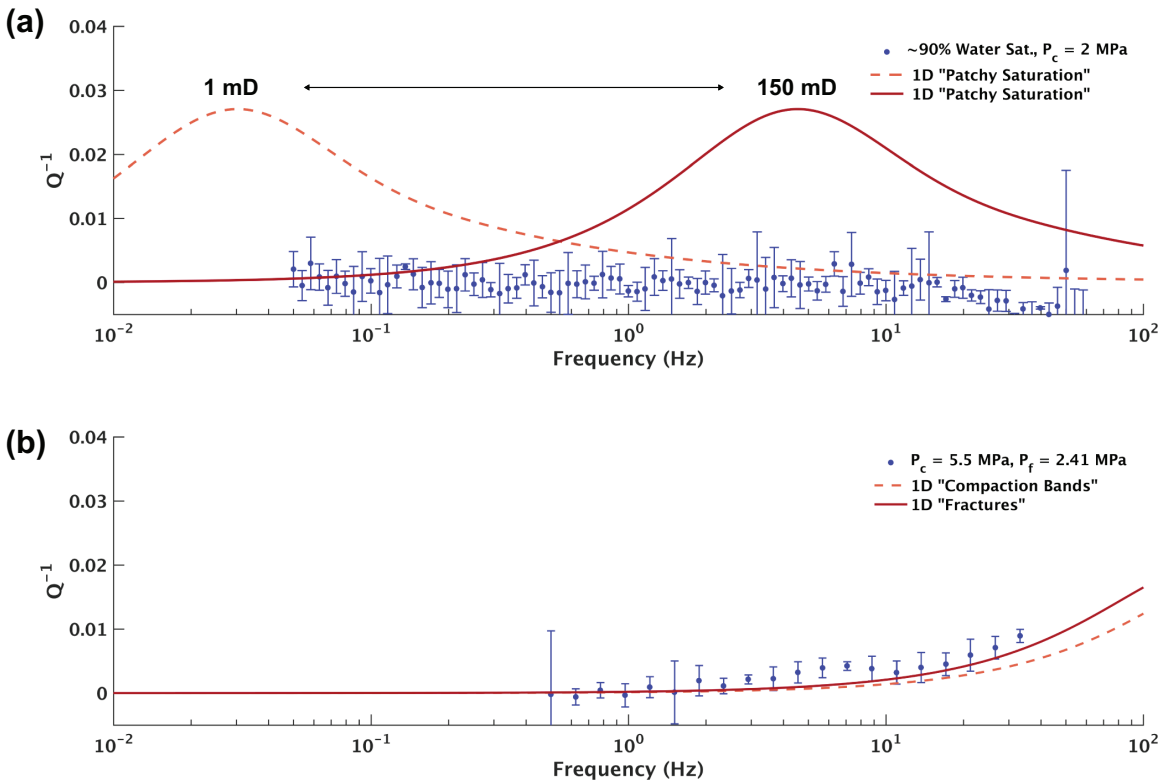

Figure 7 (a) Attenuation Q^{-1} measured from 0.05 to 50 Hz at ~90% water saturation and 2 MPa confining pressure. The results of White's model considering 90% water saturation and a homogenous solid frame with permeabilities of 1 (dashed line) and 150 mD (solid line). The thicknesses of the water- and air-saturated layers of 0.45 m and 0.05 m, respectively, are representative of the undrained sample at 90% water saturation and yield the lowest transition frequency. (b) Measured attenuation at full water saturation and 3 MPa effective stress. This data set is also presented in Fig. 5. The results of White's model consider periodic distributions of 'fractures' (solid line) and 'compaction bands' (dashed line) with water as the saturating fluid. The fractures have a thickness of 0.1 mm and the background matrix thickness is 38 mm. The latter corresponds to the sample's radius and provides the lowest transition frequency. The compaction bands have a thickness of 1 mm and the background matrix thickness is 5 mm, which is roughly consistent with the values observed in the micro-CT images. The utilized fluid and rock physical properties are listed in Tables B1–B3 in Appendix B.

that the analytical solution assumes a structurally homogenous rock, while the sample GL2 is structurally heterogeneous. The bulk and shear moduli were chosen to reflect an undamaged frame with a Poisson's ratio of 0.1. This is stiffer than the damaged sample, but influencing primarily the magnitude of the attenuation, which is not particularly relevant in this analysis. We consider the permeability of the damaged and undamaged sample, which correspond to the lowest and highest possible permeabilities measured in sample GL2. Further details with regard to the used model parameters can be found in Appendix B. The fact that the measured attenuation at 90% water saturation is negligible (Fig. 7a) in the frequency range predicted by the analytical results suggests that WIFF in response to a patchy fluid distribution is absent in sample GL2 at these frequencies. Additionally, when attenuation caused by WIFF in response to a patchy fluid distribution manifests itself, even though the largest amplitude often appears at larger water saturations such as 95–99% (Chapman *et al.* 2016), it still exhibits reasonable amplitudes and frequency dependence at saturations down to at least 80% (e.g. Tisato and Madonna 2012).

It is not immediately clear why WIFF in response to patchy saturation is not observed in sample GL2 across such a broad frequency range. Unlike the Berea sandstones studied by Tisato and Quintal (2013) and Chapman *et al.* (2016), sample GL2 has fractures and compaction bands (Fig. 3). When partially saturating the sample by imbibition, the water could be expected to form preferential flow paths along the highly permeable fractures and around the less permeable compaction bands (Baraka-Lokmane, Teutsch and Main 2001; David, Menendez and Mengus 2008; Karpyn *et al.* 2009). As a result, the distribution of the water and gas could be far more

homogenous than the decreasing water saturation with sample length inferred by Tisato and Quintal (2013) in Berea sandstone. A homogenous distribution of the water and gas at the sample scale implies that the length scale of the fluid heterogeneities in GL2 should be very small. As a consequence, attenuation caused by a patchy water distribution would occur beyond the upper limit of the measured frequency, irrespective of the sample's low permeability. Cadoret, Mavko and Zinszner (1998) came to a similar conclusion for observations of attenuation at sonic frequencies for partially saturated limestone. In this case the patch length variation was attributed to the saturation method. Another possible reason for the absence of WIFF due to patchy saturation may arise from the small pore size (~ 5 μm) of GL2, which could facilitate the formation of a stiff meniscus between the two saturating phases. In such a case a permanent pressure jump occurs between the two phases, which impedes the diffusion of wave-induced pressure gradients and as a result reduces the frequency-dependent attenuation (Tserkovnyak and Johnson 2003; Qi *et al.* 2014a; Qi, Müller and Rubino 2014b). A combination of a homogenous distribution of the water and gas and a high surface stiffness at the water–gas contact, possibly further compounded by the presence of compaction bands, may explain why we do not observe frequency-dependent attenuation in response to patchy saturation in sample GL2.

4.3 WIFF: rock matrix heterogeneities

Another form of WIFF arises from compressibility contrasts in the sample's frame (e.g. Brajanovski, Gurevich and Schoenberg 2005). The compressibility of the sample will be sensitive to the effective stress applied. In response to raising the effective stress, for example the fractures in the sample will close and/or the compaction bands will be further compressed making the sample stiffer and reducing the attenuation due to WIFF. We observe the possible left-hand side of a bell-shaped attenuation curve when the sample is 95% water-saturated and subjected to an effective stress of 1.6 MPa (Fig. 4a, orange curve). For the same water content and an effective stress of 9.4 MPa, the measured attenuation is negligible (Fig. 4b, orange curve). Since the compressibility contrast is associated with the sample's frame, frequency-dependent attenuation can also occur when the sample is fully water-saturated. Indeed, we observe the possible left-hand side of a bell-shaped attenuation curve when the sample is fully water-saturated and subjected to an effective stress of ~ 3 MPa (Fig. 5a, red curve). Again, we observe that, at higher effective stresses and full water saturation, the measured attenuation is negligible (Figs 5b,c, red curves).

To get a first-order approximation of the frequency-dependent attenuation associated with WIFF from compressibility contrasts in the sample's frame we again use White's model (White, Mikhaylova and Lyakhovitskiy 1975). Here, instead of assuming a periodic distribution in the fluid properties, we assume full water saturation and a periodic distribution of the rock frame properties to simulate the presence of either fractures or compaction bands. The fractures and compaction bands are assumed to be very compliant with respect to the embedding matrix. Details with regard to the used model parameters can be found in Appendix B. We do not intend to fit the data with the analytical model because the chosen rock physical properties are not well constrained. The analytical results are only used for a rough estimate of the transition frequency associated with each type of heterogeneity. In Fig. 7b, we show the measured attenuation at full water saturation and 3 MPa effective stress together with the analytical results. The analytical results for both fractures and compaction bands predict a transition frequency above 200 Hz, which agrees with the general trend observe in the data.

4.4 Overlap of two attenuation mechanisms

The frequency-dependent attenuation observed at full water saturation (Fig. 5a, red curve) is attributed to WIFF in response to heterogeneities in the sample's solid frame. Conversely, the low transition frequency measured at near full water saturation (Fig. 5, blue curves), when partial saturation was achieved by gas exsolution, is unlikely to be associated with any form of WIFF, as already discussed. It is therefore caused by a different and possibly independent physical mechanism. We will try to show that these two mechanisms may overlap when ~ 99 % water saturation is achieved by imbibition (Fig. 4a, red curve).

Johnston, Toksöz and Timur (1979) discussed for ultrasonic measurements that the attenuation measured in dry sandstone, at ambient humidity conditions, likely persisted in the saturated rock. Tisato and Quintal (2013) extended this discussion to seismic frequencies where the frequency-independent attenuation measured in the dry sample and the frequency-dependent attenuation observed in the partially saturated sample were in response to two mechanisms that are independent of each other. The measured attenuation in the partially saturated sample could be composed of the sum of the frequency-dependent and frequency-independent

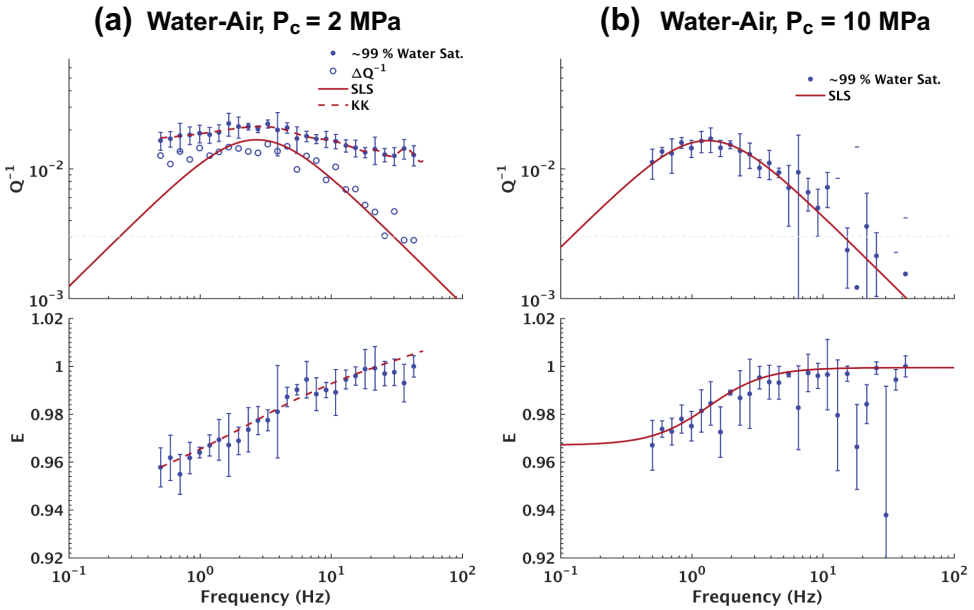

Figure 8 (a) Attenuation Q^{-1} and normalized Young's modulus E measured at ~99% water saturation and difference of the attenuation ΔQ^{-1} measured at ~99% and ~95% water saturation at 2 MPa confining pressure. (b) Attenuation measured at ~99% water saturation at 10 MPa confining pressure. The solid and dashed red lines denote the fits of the SLS and Kramers–Kronig relations (KK), respectively. The experimental data were previously presented in Fig. 4.

attenuation mechanisms. Tisato and Quintal (2014) provided further experimental support for this hypothesis.

If the two mechanisms that we observe are independent of each other, then it should be possible to isolate one from the other by subtracting the measurements where a single mechanism is present from those where both mechanisms are present. To illustrate this, we subtract the attenuation measured at ~95% water saturation, which we assume to be entirely due to WIFF associated with the frame's heterogeneity, from the attenuation measured at ~99% water saturation, which is possibly due to the overlap of two mechanisms (Fig. 4a). Figure 8a shows the resulting difference ΔQ^{-1} together with the attenuation measured at ~99% water saturation. We observe that the high-frequency asymptote of ΔQ^{-1} now scales as $Q^{-1} \propto f^{-1}$, as the SLS model fit shows. The slope is significantly steeper than that of the high-frequency asymptote of the attenuation measured at ~99% water saturation and 2 MPa confining pressure. The attenuation measured at ~99% water saturation and 10 MPa confining pressure (Fig. 8b), which is not affected by frame heterogeneities, also agrees well with the SLS model. The $Q^{-1} \propto f^{-1}$ scaling of the attenuation (Figs. 6 and 8b) together with its sensitivity to fluid pressure (Fig. 5) suggests that the frequency-dependent attenuation with transition frequencies between 1 and 5 Hz could be related to WIGED (Chapman *et al.* 2017).

We observe the overlap of the two attenuation mechanisms only when near full water saturation is achieved by imbibition (Fig. 4) and not when the gas is allowed to come out of solution in the form of pore-scale bubbles from an initially fully water-saturated state (Figs. 5 and 6). As pointed out earlier, it is possible that, during imbibition, preferential flow paths form along the more permeable fractures and around the less permeable compaction bands (Baraka-Lokmane, Teutsch and Main 2001; David, Menendez and Mengus 2008) (Fig. 3). Once these flow paths are established, simply flushing more water through the sample cannot further increase the water saturation. Therefore, the fluid pressure in the sample was increased to force the water into the remaining unsaturated pore space. It is possible that the residual gas partially dissolved into the water and came out of solution again when the pore pressure was reduced before performing the measurements. Imbibition was performed at 10 MPa confining pressure, when the majority of fractures were likely closed. When the confining pressure was lowered (Fig. 4a), the fractures opened and drew in water from the surrounding pore space, probably resulting in fully saturated fractures and a matrix containing both water and pore scale bubbles. This in turn could have resulted in the overlap of the two attenuation mechanisms (Fig. 4b, red curve, and Fig. 8). On the other hand, when partial saturation was achieved by gas

exsolution (Fig. 5a), pore-scale gas bubbles would have formed in both the fractures and the matrix. In this case, the effective bulk modulus of the fluid in the fractures would be an order-of-magnitude lower than that of water (Wood 1955), thus inhibiting the flow of water from the fractures into the background matrix (Kong *et al.* 2013). Consequently, there would be no attenuation associated with WIFF due to heterogeneities in the solid frame.

4.5 WIGED: homogenous distribution of pore-scale bubbles

So far, we have discussed the observed attenuation mainly in terms of fluid pressure diffusion induced by compressibility contrasts, which, in turn, causes energy dissipation by WIFF. Another possible mechanism is the dissolution-exsolution of gas bubbles or WIGED, which was first explored by Tisato *et al.* (2015). WIGED dissipates seismic wave energy by moving the gas molecules in the bubbles into and out of solution with the surrounding water. Tisato *et al.* (2015) modelled the attenuation caused by WIGED with a finite difference scheme that solves the equations describing the exchange rate of gas molecules between a single spherical bubble and the surrounding spherical shell of water and the associated rate of change in the bubble radius (e.g., Holocher *et al.* 2003; Liang *et al.*, 2011). From the incremental change in volume and the applied stress, the complex fluid bulk modulus of the bubble-liquid system can be calculated. Subsequently, Gassmann fluid substitution (Gassmann 1951) can be used to determine the complex bulk modulus of the saturated rock.

It is not clear whether the bell-shaped attenuation curves, with peaks at 1–5 Hz, which are observed when the gas is allowed to come out of solution (Figs. 5 and 6), are caused by WIGED. However, our results are consistent with a number of observations made for similar experiments on Berea sandstone samples where partial saturation was also achieved by gas exsolution (Tisato *et al.* 2015; Chapman *et al.* 2017). The main difference between those experiments and our current study is the type of porous material employed. The sample GL2 considered in this study was made of sintered borosilicate glass and characterized by a very high porosity and very small pore size. Moreover, the sample became structurally heterogeneous throughout the consecutive sets of experiments. In spite of this, the attenuation peaks measured in sample GL2 lie in a comparable frequency range as those observed for the Berea sandstone samples, which were located between 1 and 10 Hz. The decrease in attenuation magnitude with increasing fluid pressure (Fig. 5) was also previously observed. The attenuation does neither appear to be strongly influenced by changes in effective stress (Fig. 5) nor by the type of gas used (air, nitrogen or carbon dioxide) (Fig. 6). However, these experiments would require a more controlled experimental protocol to allow for a quantification of the amount of dissolved gas in the liquid. An additional and consistent similarity between our results and those reported by the previous studies is the frequency scaling of the attenuation when partial saturation is achieved by gas exsolution (Chapman *et al.* 2017), which is generally well described by an SLS model with a single relaxation time (Fig. 6).

There are some observations in our current study that differ from those made in the related experiments on samples of Berea sandstone. Although the decrease in attenuation magnitude with increasing fluid pressure is consistent with earlier observations, the associated shift of the attenuation peak to higher frequencies was previously not observed (Fig. 5). Also, it is not clear how to reconcile a bubble diameter of 18 μm used as a fitting parameter in the interpretation of Tisato *et al.* (2015) given that the pore size of sample GL2 is only $\sim$5 μm. Observations made by Zuo *et al.* (2017) and Xu *et al.* (2017) for carbon dioxide exsolution raise important questions with regard to the role of the pore size and structure as well as the pressure depletion rate on the size and distribution of gas bubbles nucleating in the pore space. The process of gas exsolution is more complex than anticipated and an improved understanding thereof could not only have interesting implications for improving the understanding of the WIGED (Tisato *et al.* 2015) and patchy saturation mechanisms (Masson and Pride 2007, 2011; Müller, Toms-Stewart and Wenzlau 2008), but also for better constraining effects of trapped gas bubbles on the hydraulic conductivity of a porous medium.

5. CONCLUSIONS

We used the forced oscillation method to measure the extensional-mode attenuation and Young's modulus dispersion in the seismic frequency range on a porous sample made of sintered borosilicate glass. The experiments were performed on the dry as well as partially and fully water-saturated sample at effective stresses up to 10 MPa. Partial water saturation was achieved by imbibition from an initially dry state as well as by gas exsolution from an initially fully water-saturated state.

The sample underwent progressive permanent deformation over the course of the experiments in response to the applied effective and static axial stresses, in the form of mesoscopic fractures and compaction bands. Meanwhile, the measured frequency-dependent attenuation and Young's modulus are in agreement with the causality principle stipulated by the

Kramers–Kronig relations. This indicates that the permanent deformation of the sample did not predominantly occur in response to the forced axial oscillations of the sample.

The left-hand side of a possible bell-shaped attenuation curve is observed at 95% and at full water saturation as well as at effective stresses lower than 3 MPa with a transition frequency beyond the upper limit of the experimental frequency range. The observed trends of the attenuation with effective stresses are consistent with wave-induced fluid flow or WIFF in response to compressibility contrasts within the solid frame of the sample, possibly associated with the fractures and/or compaction bands that formed over the course of the experiments.

Close to full water saturation (~99% water), bell-shaped attenuation curves with transition frequencies between 1 and 5 Hz are observed when partial saturation was achieved by imbibition and by gas exsolution. The governing attenuation mechanism is sensitive to changes in fluid pressure and largely insensitive to changes in the effective stress. The latter excludes WIFF as the attenuation mechanism and implies that the attenuation is unaffected by the structural changes in the solid frame of the sample. These observations indicate that the attenuation mechanism is predominantly dependent on the properties of the saturating fluid. Furthermore, the frequency dependence of the measured attenuation corresponds to that of an SLS model with a single relaxation time. These observations are generally consistent with those previously made for samples of Berea sandstone, for which wave-induced gas exsolution–dissolution or WIGED was proposed as the likely attenuation mechanism.

ACKNOWLEDGEMENTS

This work is supported by a grant from the Swiss National Science Foundation. We thank Jean-Pierre Burg for access to the ETH Zurich Rock Deformation Laboratory and Robert Hofmann for competent technical support. We also thank Marie Violay for access to the EPFL Laboratory of Experimental Rock Mechanics and Laurent Gastaldo for helping with remedial porosity and permeability measurements. All the data presented in this article are available by contacting the authors.

REFERENCES

Adam L., Batzle M., Lewallen K.T. and van Wijk K. 2009. Seismic wave attenuation in carbonates. *Journal of Geophysical Research* **114**, B06208.

Baraka-Lokmane S., Teutsch G. and Main I.G. 2001. Influence of open and sealed fractures on fluid flow and water saturation in sandstone cores using magnetic resonance imaging. *Geophysical Journal International* **147**, 263–271.

Batzle M.L., Han D.-H. and Hofmann R. 2006. Fluid mobility and frequency-dependent seismic velocity – Direct measurements. *Geophysics* **71**, N1–N9.

Borgomano J.V.M., Pimienta L., Fortin J. and Gueguen Y. 2017. Dispersion and attenuation measurements of elastic moduli of a dual-porosity limestone. *Journal of Geophysical Research: Solid Earth* **122**, https://doi.org/10.1002/2016JB013816.

Brajanovski M., Gurevich B. and Schoenberg M. 2005. A model for P-wave attenuation and dispersion in a porous medium permeated by aligned fractures. *Geophysical Journal International* **163**, 372–384.

Cadoret T., Marion D. and Zinszner B. 1995. Influence of frequency and fluid distribution on elastic wave velocities in partially saturated limestones. *Journal of Geophysical Research* **100**, 9789–9803.

Cadoret T., Mavko G. and Zinszner B. 1998. Fluid distribution effect on sonic attenuation in partially saturated limestones. *Geophysics* **63**, 154–160.

Chapman M., Zatspin S.V. and Crampin S. 2002. Derivation of a microstructural poroelastic model. *Geophysical Journal International* **151**, 427–451.

Chapman S., Tisato N., Quintal B. and Holliger K. 2016. Seismic attenuation in partially saturated Berea sandstone submitted to a range of confining pressures. *Journal of Geophysical Research: Solid Earth* **121**, 1664–1676.

Chapman S., Tisato N., Quintal B. and Holliger K. 2017. Frequency scaling of seismic attenuation in rocks saturated with two fluids phases. *Geophysical Journal International* **208**, 221–225.

David C., Menendez B. and Mengus J-M. 2008. Influence of mechanical damage on fluid flow patterns investigated using CT scanning imaging and acoustic emissions techniques. *Geophysical Research Letters* **35**, L16313.

Dunn K.-J. 1987. Sample boundary effect in acoustic attenuation of fluid-saturated porous cylinders. *Journal of the Acoustical Society of America* **81**, 1259–1266.

Dutta N.C. and Seriff A.J. 1979. On White's model of attenuation in rocks with partial gas saturation. *Geophysics* **44**, 1806–1812.

Gardner G.H.F. 1962. Extensional waves in fluid-saturated porous cylinders. *Journal of the Acoustical Society of America* **34**, 36–40.

Gassmann, F. 1951. Über die Elastizität poröser Medien. *Vierteljahrsschrift der Naturforschenden Gesellschaft in Zürich* **96**, 1–23.

Gautam K. 2003. *Fluid effects on attenuation and dispersion of elastic waves*. Master thesis, Colorado School of Mines, Colorado.

Gurevich B., Makaryska D., de Paula O.S. and Pervukhina M. 2010. A simple model for squirt-flow dispersion and attenuation in fluid-saturated granular rocks. *Geophysics* **75**, N109–N120.

Holcomb D.J. and Olsson W.A. 2003. Compaction localization and fluid flow. *Journal of Geophysical Research* **108**(B6), 2290.

Holocher J., Peters F., Aeschbach-Hertig W., Kinzelbach W. and Kipfer, R. 2003. Kinetic model of gas bubble dissolution in groundwater and its implications for the dissolved gas composition. *Environmental Science and Technology* **37**, 1337–1343.

Johnston D.H., Toksöz M.N. and Timur A. 1979. Attenuation of seismic waves in dry and saturated rocks: II. Mechanisms. *Geophysics* **44**, 691–711.

Karpyn Z.T., Alajmi A., Radaelli F., Halleck P.M. and Grader A.S. 2009. X-ray CT and hydraulic evidence for a relationship between fracture conductivity and adjacent matrix porosity. *Engineering Geology* **103**, 139–145.

Kong L., Gurevich B., Müller T.M., Wang Y. and Yang H. 2013. Effect of fracture fill on seismic attenuation and dispersion in fractured porous rocks. *Geophysical Journal International* **195**, 1679–1688.

Krzikalla F. and Müller T.M. 2011. Anisotropic P-SV-wave dispersion and attenuation due to inter-layer flow in thinly layered porous rocks. *Geophysics* **76**, WA135–WA145.

Lakes R. 2009. *Viscoelastic Materials*. Cambridge University Press.

Liang, J.-H., McWilliams J.C., Sullivan P.P. and Baschek B. 2011. Modeling bubbles and dissolved gases in the ocean. *Journal of Geophysical Research* **116**, C03015.

Liu H.-P., Anderson D.L. and Kanamori H. 1976. Velocity dispersion due to anelasticity; implications for seismology and mantle composition. *Geophysical Journal International* **47**, 41–58.

Masson Y.J. and Pride S.R. 2007. Poroelastic finite difference modeling of seismic attenuation and dispersion due to mesoscopic-scale heterogeneity. *Journal of Geophysical Research* **112**, B03204.

Masson Y.J. and Pride S.R. 2011. Seismic attenuation due to patchy saturation. *Journal of Geophysical Research* **116**, B03206.

Mavko G. and Jizba D. 1991. Estimating grain-scale fluid effects on velocity dispersion in rocks. *Geophysics* **56**, 1940–1949.

Mavko G., Mukerji T. and Dvorkin J. 2009. *The Rock Physics Handbook*. Cambridge University Press.

McKavanagh B. and Stacey F.D. 1974. Mechanical hysteresis in rocks at low strain amplitudes and seismic frequencies. *Physics of the Earth and Planetary Interiors* **8**, 246–250.

Mikhaltsevitch V., Lebedev M. and Gurevich B. 2016a. Validation of the laboratory measurements at seismic frequencies using the Kramers-Kronig relationship. *Geophysical Research Letters* **43**, 4986–4991.

Mikhaltsevitch V., Lebedev M. and Gurevich B. 2016b. Laboratory measurements of the effect of fluid saturation on elastic properties of carbonates at seismic frequencies. *Geophysical Prospecting* **64**, 799–809.

Mörig R. and Burkhardt H. 1989. Experimental evidence for the Biot–Gardner theory. *Geophysics* **54**, 524–527.

Müller T.M., Gurevich B. and Lebedev M. 2010. Seismic wave attenuation and dispersion resulting from wave-induced flow in porous rocks – A review. *Geophysics* **75**, A147–A164.

Müller T.M., Toms-Stewart J. and Wenzlau F. 2008. Velocity-saturation relation for partially saturated rocks with fractal pore fluid distribution. *Geophysical Research Letters* **35**, L09306.

Pimienta L., Borgomano J.V.M., Fortin J. and Guéguen Y. 2016. Modelling the drained/undrained transition: effect of the measuring method and the boundary conditions. *Geophysical Prospecting* **64**, 1098–1111.

Pimienta L., Fortin J. and Guéguen Y. 2015. Bulk modulus dispersion and attenuation in sandstones. *Geophysics* **80**(2), D111–D127.

Qi Q., Müller T.M., Gurevich B., Lopes S., Lebedev M. and Caspari E. 2014a. Quantifying the effect of capillarity on attenuation and dispersion in patchy-saturated rocks. *Geophysics* **79**, WB35–WB50.

Qi Q., Müller T.M. and Rubino J.G. 2014b. Seismic attenuation: effects of interfacial impedance on wave-induced pressure diffusion. *Geophysical Journal International* **199**, 1677–1681.

Quintal B. 2012. Frequency-dependent attenuation as a potential indicator of oil saturation. *Journal of Applied Geophysics* **82**, 119–128.

Quintal B., Jaenicke R., Rubino J.G., Steeb H. and Holliger K. 2014. Sensitivity of S-wave attenuation to the connectivity of fractures in fluid-saturated rocks. *Geophysics* **79**, WB15–WB24.

Spencer J.W. and Shine J. 2016. Seismic wave attenuation and modulus dispersion in sandstones. *Geophysics* **81**, D211–D231.

Subramaniyan S., Quintal B., Madonna C. and Saenger E.H. 2015. Laboratory-based seismic attenuation in Fontainebleau sandstone: evidence of squirt flow. *Journal of Geophysical Research: Solid Earth* **120**, 7526–7535.

Tisato N. and Madonna C. 2012. Attenuation at low seismic frequencies in partially saturated rocks: measurements and descriptions of a new apparatus. *Journal of Applied Geophysics* **86**, 44–53.

Tisato N. and Quintal B. 2013. Measurements of seismic attenuation and transient fluid pressure in partially saturated Berea sandstone: evidence of fluid flow on the mesoscopic scale. *Geophysical Journal International* **195**(1), 342–351.

Tisato N. and Quintal B. 2014. Laboratory measurements of seismic attenuation in sandstone: strain versus fluid saturation effects. *Geophysics* **79**, WB9–WB14.

Tisato N., Quintal B., Chapman S., Podladchikov Y. and Burg J.-P. 2015. Bubbles attenuate elastic waves at seismic frequencies: first experimental evidence. *Geophysical Research Letters* **42**, 3880–3887.

Tserkovnyak Y. and Johnson D.B. 2003. Capillary forces in the acoustics of patchy-saturated media. *Journal of the Acoustical Society of America* **114**, 2596–2606.

Vajdova V., Baud P. and Wong T-f. 2004. Permeability evolution during localized deformation in Bentheim sandstone. *Journal of Geophysical Research* **109**, B10406.

White J.E. 1975. Computed seismic speeds and attenuation in rocks with partial gas saturation. *Geophysics* **40**, 224–232.

White J.E., Mikhaylova N.G. and Lyakhovitskiy F.M. 1975. Low-frequency seismic waves in fluid-saturated layered rocks. *Izvestija Academy of Sciences USSR, Physics of the Solid Earth* **11**, 654–659.

Wong T.-f., Baud P. and Klein E. 2001. Localized failure modes in a compactant porous rock. *Geophysical Research Letters* **28**, 2521–2524.

Wood A.B. 1955. *A Textbook of Sound*. New York: The MacMillan Company.

Xu R., Li R., Huang F. and Jiang P. 2017. Pore-scale visualization on a depressurization-induced CO_2 exsolution. *Science Bulletin* **62**, 795–803.

Zener C. 1948. *Elasticity and Anelasticity of Metals*. Chicago, IL: University of Chicago Press.

Zuo L., Ajo-Franklin J.B., Voltolini M., Geller J.G. and Benson S.M. 2017. Pore-scale multiphase flow modeling and imaging of CO2 exsolution in Sandstone. *Journal of Petroleum Science and Engineering* **155**, 63–77.

APPENDIX A

Figure A1 shows the individual measurement cycles of attenuation and Young's modulus for the experiments with air, nitrogen and carbon dioxide as the saturating gases (Fig. 6). For the experiments involving air and nitrogen, there is no visible trend over the five cycles. The experiment with carbon dioxide (Figs. 6c and A1c), however, shows a moderate reduction in the Young's modulus over the course of the five measurement cycles. The Young's modulus is normalized with respect to its mean value measured during the first cycle that amplifies this trend. Inspecting the same data set that is

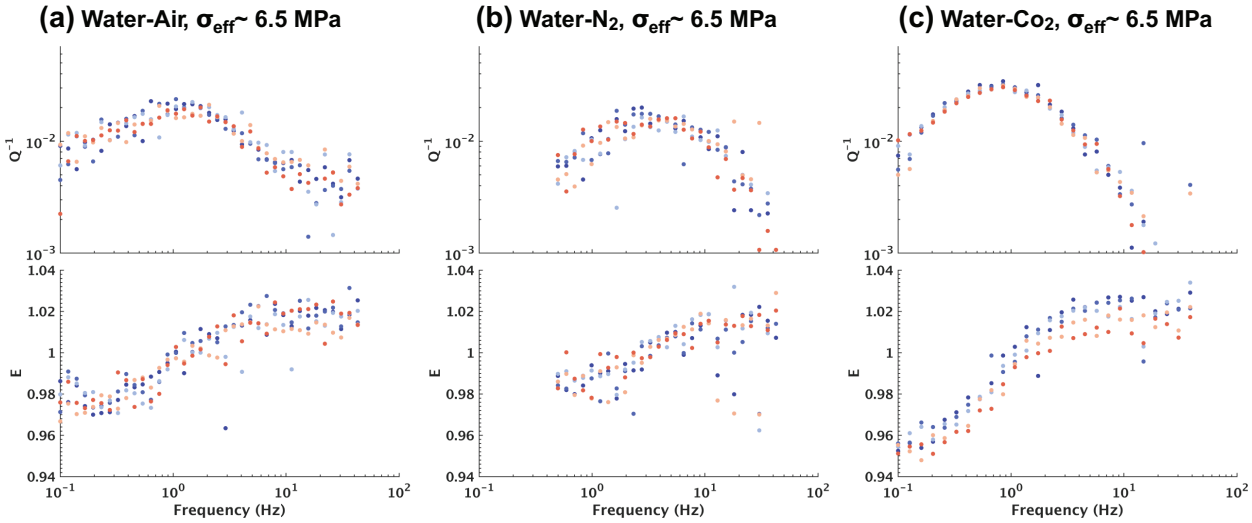

Figure A1 Attenuation Q^{-1} and normalized Young's modulus E at near full water saturation and a constant effective stress σ_{eff} of ~6.5 MPa (Figure 6). The Young's modulus is normalized against its mean value measured during the first cycle of measurements. Each colour corresponds to one cycle of measurements, the order being from dark blue (first) to dark red (fifth). The grey shaded area denotes the limit of the measurement sensitivity.

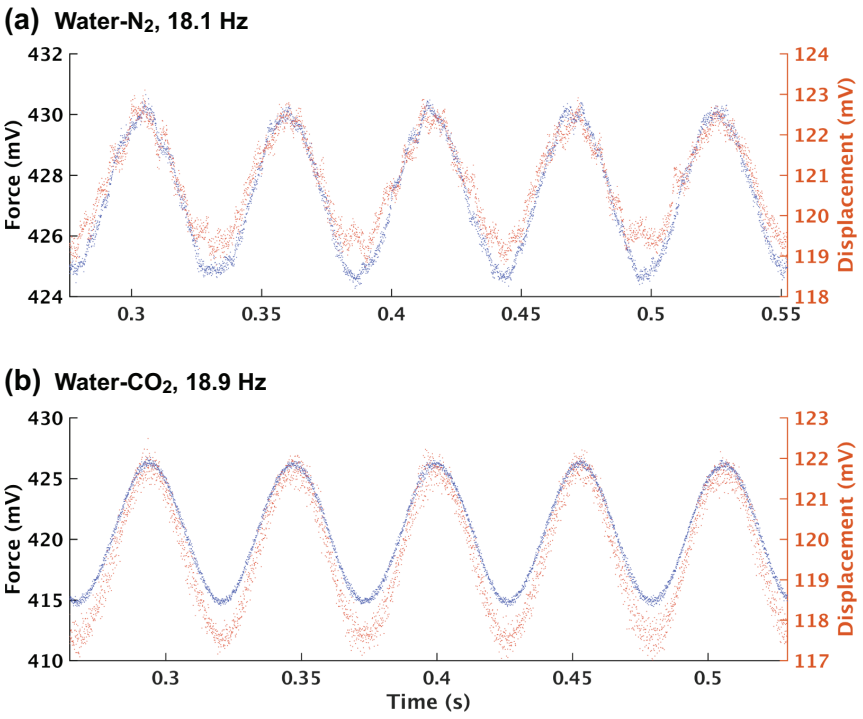

Figure A2 Unprocessed signals from the load cell and strain-gauge cantilever corresponding to the force and displacement of the sample, respectively. (a) Oscillations at 18.1 Hz associated with the data presented in Fig. 6b for nitrogen. (b) Oscillations at 18.9 Hz from data presented in Fig. 6c for carbon dioxide.

shown in its non-normalized form in Fig. 5b, we observe that the range of the Young's modulus values is small, indicating that a possible weakening of the solid frame during the experiment is likely to be negligible. All the other experiments, which involve carbon dioxide (Fig. 5), were also checked for similar trends. For the measurements at 3 MPa effective stress and 0.06 MPa fluid pressure (Fig. 5a, blue curve), the later measurement cycles tend to show a slightly elevated Young's modulus. All other measurements presented in Fig. 5 show no visible trend, which suggests that, in general, no permanent deformation of the sample took place during the actual forced oscillation measurements.

Figure A2 shows the unprocessed signals from the load cell and the strain-gauge cantilever recorded during the

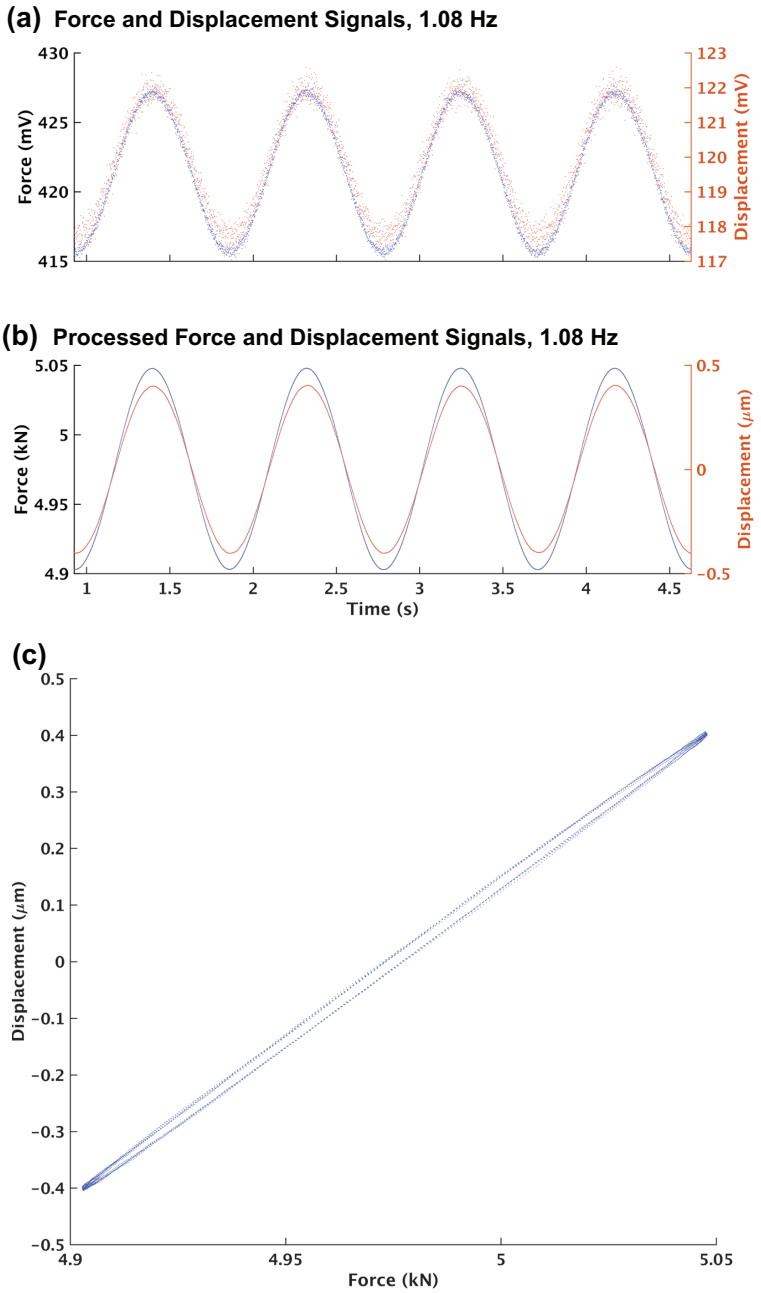

Figure A3 Signals from the measurements with carbon dioxide for oscillations at 1.08 Hz that correspond to the peak attenuation measured and presented in Fig. 6c. (a) Unprocessed signals from the load cell and strain-gauge cantilever and (b) corresponding processed signals. (c) Force versus displacement ellipse.

experiments with nitrogen (Figs. 6b and A1b) and carbon dioxide (Figs. 6c and A1c) for imposed oscillating stresses of 18.1 Hz and 18.9 Hz, respectively. The stress and displacement signals are unstable for the experiments with nitrogen (Fig. A2a) as evidenced by the broad scatter of the inferred values for the attenuation and Young's modulus presented in Figs. 6b and A1b. The reason for this is that the displacement of the sample does not recover from the applied stress. This in turn suggests that the sample was permanently deformed in response to the forced oscillation at 18.1 Hz. Conversely, there is no evidence for permanent deformation during the corresponding measurements with carbon dioxide as the gas phase (Figs. A1c and A2b).

Figure A3 shows the unprocessed and processed signals from the load cell and strain-gauge cantilever recorded during the experiments with carbon dioxide (Fig. 6c). The frequency of the oscillations is 1.08 Hz, at which the maximum attenuation was observed. The signal shows little noise in its unprocessed form and the sample displacement recovers when the load is at its minimum. The force-displacement graph (Fig. A3c) shows an ellipse consistent with a linear response for a sinusoidal loading (e.g. Lakes 2009).

APPENDIX B

To get a first-order approximation of the attenuation in response to WIFF caused by patchy saturation and compressibility contrasts in the solid matrix we use White's 1D analytical solution for interlayer flow (White, Mikhaylova and Lyakhovitskiy 1975). More specifically, we use the corresponding formulation of Quintal (2012) that provides the complex P-wave modulus of a wave traveling perpendicular to the layers. To evaluate the complex Young's modulus from the P-wave modulus we use Krzikalla and Müller's (2011) extension of the analytic solution.

The bulk and shear moduli are chosen to reflect an undamaged frame, with a Poisson's ratio of 0.1, which is stiffer than the damaged sample. These values for the bulk and shear moduli are used to reflect the properties of the background matrix for the three cases considered. The permeabilities chosen for the patchy saturation case reflect the permeability of the intact and deformed sample. The permeability of the background matrix for the fractures is chosen to reflect the permeability of the damaged frame at 3 MPa effective stress (Table 1). Conversely, the permeability of the background matrix for the compaction bands reflects the permeability of the undamaged sample, assuming that the overall reduction in permeability is in response to the formation of the compaction bands. The fractures are approximated as compliant and highly permeable thin layers using the parameters from Quintal *et al.* (2014). For the compaction bands, we use the Herz–Mindlin model for spherical grain packing (e.g. Mavko *et al.* 2009) to approximate the effective bulk and shear moduli from the Young's modulus and the Poisson ratio of borosilicate, 64 GPa and 0.2, respectively. The permeability of the compaction bands was estimated from the permeability measured in the remaining sample pieces at high effective stresses (Table 2). The thickness of the fractures is 0.1 mm and the background matrix thickness is 38 mm, which corresponds to the sample's radius and provides the lowest transition frequency. The compaction bands have a thickness of 1 mm and the background matrix thickness is 5 mm, which correspond approximately to the values observed in the micro-CT images. All rock physical properties used in the respective models can be found in Tables B1, B2 and B3.

Table B1 Rock physical properties of the background matrix used in the extended 1D analytical solution of White's model to simulate the WIFF effects in response to patchy saturation and heterogeneities in the solid frame related to fractures and compaction bands

Parameters	Intact matrix 'Patchy Saturation'	Embedding matrix 'Fractures'	Intact matrix 'Compaction Bands'
Grain Bulk modulus (GPa)	36	36	36
Bulk modulus (GPa)	8.33	8.33	8.33
Shear modulus (GPa)	9.1	9.1	9.1
Porosity	0.44	0.45	0.45
Permeability (mD)	1–150	15	150

Table B2 Rock physical properties of the fractures and compaction bands in the extended 1D analytical solution of White's model

Parameters	Fracture[a]	Compaction Band
Grain Bulk modulus (GPa)	36	36
Bulk modulus (GPa)	0.025	0.73
Shear modulus (GPa)	0.02	0.84
Porosity	0.50	0.41
Permeability (mD)	10^4	0.1

[a]Quintal *et al.* (2014)

Table B3 Physical properties of the saturating fluids used in the extended 1D analytical solution of White's model

Parameters	Water	Air
Bulk modulus (GPa)	2.2	10^{-4}
Viscosity (Pa × s)	0.001	2×10^{-5}